Inorganic Chemistry

Article

pubs.acs.org/IC

Molecular Magnetism of M_6 Hexagon Ring in D_{3d} Symmetric $[(MCl)_6(XW_9O_{33})_2]^{12-}$ (M = Cu^{II} and Mn^{II}, X = Sb^{III} and As^{III})

Toshihiro Yamase,*[†,§] Hirofumi Ishikawa,[§] Hiroko Abe,[§] Keisuke Fukaya,[§] Hiroyuki Nojiri,[‡] and Hideo Takeuchi[∥]

[†]MO device, 2-14-10 Kanaiwa-higashi, Kanazawa 920-0335, Japan

[§]Chemical Resources Laboratory, Tokyo Institute of Technology, R1-21 4259 Nagatsuta, Midori-ku, Yokohama 226-8503, Japan

[‡]Institute for Material Research, Tohoku University, 2-1-1 Katahira, Aoba-ku, Sendai 980-8577, Japan

[∥]Toyota Technological Institute, 2-12-1 Hisakata, Tempaku-ku, Nagoya 468-8511, Japan

Supporting Information

ABSTRACT: Ferromagnetic $[n\text{-}BuNH_3]_{12}[(CuCl)_6(SbW_9O_{33})_2]\cdot 6H_2O$ (**1**) and antiferromagnetic $[n\text{-}BuNH_3]_{12}[(MnCl)_6(AsW_9O_{33})_2]\cdot 6H_2O$ (**4**) have been synthesized and structurally and magnetically characterized. Two complexes are structural analogues of $[n\text{-}BuNH_3]_{12}[(CuCl)_6(AsW_9O_{33})_2]\cdot 6H_2O$ (**2**) and $[n\text{-}BuNH_3]_{12}[(MnCl)_6(SbW_9O_{33})_2]\cdot 6H_2O$ (**3**) with their ferromagnetic interactions, first reported by us in 2006.[1] When variable temperature (T) direct current (dc) magnetic susceptibility (χ_M) data are analyzed with the isotropic exchange Hamiltonian for the magnetic exchange interactions, $\chi_M T$ vs T curves fitted by a full matrix diagonalization (for **1**) and by the Kambe vector coupling method/Van Vleck's approximation (for **4**) yield J = +29.5 and −0.09 cm^{-1} and g = 2.3 and 1.9, respectively. These J values were significantly distinguished from +61.0 and +0.14 cm^{-1} for **2** and **3**, respectively. The magnetization under the pulsed field (up to 10^3 T/s) at 0.5 K exhibits hysteresis loops in the adiabatic process, and the differential magnetization (dM/dB) plots against the pulsed field display peaks characteristic of resonant quantum tunneling of magnetization (QTM) at Zeeman crossed fields, indicating single-molecule magnets for **1**−**3**. High-frequency ESR (HFESR) spectroscopy on polycrystalline samples provides $g_{\parallel}$ = 2.30, $g_{\perp}$ = 2.19, and D = −0.147 cm^{-1} for **1** (S = 3 ground state), $g_{\parallel}$ = 2.29, $g_{\perp}$ = 2.20, and D = −0.145 cm^{-1} for **2** (S = 3), and $g_{\parallel}$ = 2.03 and D = −0.007 cm^{-1} for **3** (S = 15). An attempt to rationalize the magnetostructural correlation among **1**−**4**, the structurally and magnetically modified D_{3d}-symmetric M (=Cu^{II} and Mn^{II})$_6$ hexagons sandwiched by two diamagnetic α-B-$[XW_9O_{33}]^{9-}$ (X = Sb^{III} and As^{III}) ligands through M-(μ_3-O)-W linkages, is made. The strongest ferromagnetic coupling for the Cu_6 hexagon of **2**, the structure of which approximately provides the $Cu_6(\mu_3\text{-}O)_{12}$ cylindrical geometry, is demonstrated by the polarization mechanism based on the point-dipole approximation, which provides a decrease of the ferromagnetic interaction due to the out-of-cylinder deviation of the Cu atoms for **1**. The different nature of the magnetic exchange interaction in **3** and **4** is understood by the combined effect of the out-of plane deviation (the largest for **4**) of the Mn atoms from the $Mn(\mu_3\text{-}O)_2Mn$ least-squares plane and the antiferromagnetic contribution arising from the large Mn−O−Mn bond angle. The primary contribution to D is discussed in terms of the magnetic dipole−dipole interaction between the electrons located on the magnetic sites in the M_6 hexagon.

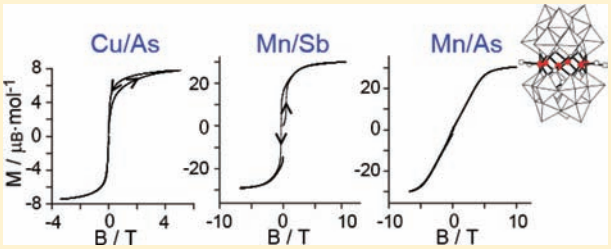

INTRODUCTION

Much attention to magnetically significant polyoxometalates is still paid as model systems for better understanding of the exchange interaction of magnetic clusters, which is very important in research areas of molecular magnetism and bioinorganic chemistry.[2] Their suitability as models is based on the following points: (i) polyoxometalates can coordinate moieties of paramagnetic ions with unusual geometries and highly symmetrical topologies at specific sites of their structures; (ii) such magnetic centers embedded in the structures are isolated from the neighboring molecules with a variety of sizes and high stability due to the diamagnetic frameworks of polyoxometalate ligands; (iii) modification of the magnetic centers is possible by modifying the structure, symmetry, and size of polyoxometalate ligands. We have shown the spin-frustrated $(VO)_3$-triangle sandwiched by two diamagnetic α-B-$[XW_9O_{33}]^{9-}$ (X = Sb^{III} and Bi^{III}) ligands in D_{3h} of the local symmetry using $[(VO)_3(SbW_9O_{33})_2]^{12-}$ and $[(VO)_3(BiW_9O_{33})_2]^{12-}$ as a simple model of the magnetization (involving the Dzyaloshinsky−Moriya interaction) between pure quantum states $S = {}^1/_2$ and $S = {}^3/_2$.[3] Together with a subsequent effort to provide clear-cut evidence for the Dzyaloshinsky−Moriya interaction inducing half step magnetization by using single crystals of $[\{Cu(H_2O)\}_3(SbW_9O_{33})_2]^{12-}$,[4] this let us start the magnetochemistry of a variety of the spin rings embedded in polyoxometalates for understanding the quantum hysteresis of spin rings at the molecular level. We have shown a ferromagnetism of the D_{3d}

Received: November 22, 2011
Published: April 2, 2012

   dx.doi.org/10.1021/ic202513q | Inorg. Chem. 2012, 51, 4606−4619

symmetric Cu_6 and Mn_6 hexagons (with S = 3 and 15 spin ground states, respectively) in $[(CuCl)_6(AsW_9O_{33})_2]^{12-}$ and $[(MnCl)_6(SbW_9O_{33})_2]^{12-}$,[1] and also shown the $^1/_3$ magnetization anomaly of the Mn_6 triangular spin-prism in $[Mn_6(H_2O)_2(AsW_9O_{34})_2(AsW_6O_{26})]^{17-}$, which originates from a delicate balance of exchange interaction.[5] In our subsequent efforts on synthesis and magnetism of magnetically significant novel polyoxometalates, $[Cu_4(GeW_9O_{34})_2]^{12-}$, consisting of a rhomb-like Cu_4-tetragon sandwiched by α-B-$[GeW_9O_{34}]^{10-}$ ligands through α-Keggin linkage, has been synthesized and a comparative investigation of its magnetochemistry with the well-known isomer of $[Cu_4(H_2O)_2(GeW_9O_{34})_2]^{12-}$ (with β-Keggin linkage) indicates that the magnetic exchange interactions of four $d_{x^2-y^2}$-electron spins in the Cu_4-tetragon can be explained by the point-dipole approximation.[6,7]

In continuation of our study on the ferromagnetism of the D_{3d}-symmetric Cu_6 and Mn_6 hexagons in $[(CuCl)_6(AsW_9O_{33})_2]^{12-}$ and $[(MnCl)_6(SbW_9O_{33})_2]^{12-}$,[1] we have investigated the magnetic properties of $[(CuCl)_6(SbW_9O_{33})_2]^{12-}$ (with S = 3 ground state) and $[(MnCl)_6(AsW_9O_{33})_2]^{12-}$ (unexpectedly with S = 0 ground state) for a better understanding of the magnetostructural chemistry of D_{3d}-symmetric M_6 hexagons in $[(MCl)_6(XW_9O_{33})_2]^{12-}$: the exchange of the X atom between $[(CuCl)_6(AsW_9O_{33})_2]^{12-}$ and $[(MnCl)_6(SbW_9O_{33})_2]^{12-}$ in the structural analogues of $[(MCl)_6(XW_9O_{33})_2]^{12-}$ provides the structural modification of a hexacapped hexagonal prism consisting of six edge-shared $ClMO_4$-square-pyramids, since a smaller angle of O–Sb–O with a longer Sb–O bond distance in a XO_3 trigonal pyramid would introduce a shorter Sb···Sb distance in $[(MCl)_6(XW_9O_{33})_2]^{12-}$. Thus, it is interesting to see how changes in M and X in $[(MCl)_6(XW_9O_{33})_2]^{12-}$ (M = Cu^{II} and Mn^{II}; X = As^{III} and Sb^{III}) modulate the magnetic exchange interactions and how this is manifested magnetostructurally. Although the ferromagnetic Cu_6 hexagon was at first reported for $[(PhSiO_2)_6Cu_6(O_2SiPh)_6]\cdot 6EtOH$ (with J = +21.0 cm^{-1}) in Cu^{II}-containing polyorganosiloxanato clusters, there has been no attempt to rationalize the magnetostructural correlation.[8] As ferromagnetic polyoxometalates, so far, 6-fold coordination transition-metals clusters such as $[Ni_4(H_2O)_2(P_2W_{15}O_{56})_2]^{16-}$,[9] $[M_4(H_2O)_2(PW_9O_{34})_2]^{10-}$ (M = Co^{II}, Ni^{II}),[7d,e] $[Co_3W_4(D_2O)_2(ZnW_9O_{34})_2]^{12-}$,[10] $[Ni_3Na(H_2O)_2(XW_9O_{34})_2]^{11-}$ (X = P^V, As^V),[11,12] $[Ni_6(H_2O)_2(AsW_9O_{34})_2(AsW_6O_{26})]^{17-}$,[12] $[Ni_4Mn_2(H_2O)_2(PW_9O_{34})_2(PW_6O_{26})]^{17-}$,[12] $[\{\gamma\text{-}SiW_{10}O_{36}Cu_2(H_2O)(N_3)_2\}_2]^{12-}$, and $[\{\gamma\text{-}SiW_8O_{31}Cu_3(OH)(H_2O)(N_3)\}_3(N_3)]^{19-}$ have been recognized, and the two isolated $[Cu_2(\mu_{1,1}\text{-}N_3)_2]$ pairs in $[\{\gamma\text{-}SiW_{10}O_{36}Cu_2(H_2O)(N_3)_2\}_2]^{12-}$ have been estimated to be most strongly ferromagnetically coupled with J = +224 cm^{-1}.[2d] However, the observed ferromagnetic behaviors have never been rationalized with magnetostructural correlations. We herein attempt to rationalize the magnetostructural correlation among the M_6 (M = Cu^{II} and Mn^{II}) hexagons in $[n\text{-}BuNH_3]_{12}[(CuCl)_6(SbW_9O_{33})_2]\cdot 6H_2O$ (**1**), $[n\text{-}BuNH_3]_{12}[(CuCl)_6(AsW_9O_{33})_2]\cdot 6H_2O$ (**2**), $[n\text{-}BuNH_3]_{12}[(MnCl)_6(SbW_9O_{33})_2]\cdot 6H_2O$ (**3**), and $[n\text{-}BuNH_3]_{12}[(MnCl)_6(AsW_9O_{33})_2]\cdot 6H_2O$ (**4**), based on the results of crystal structure, dc and ac magnetic susceptibilities, in-depth magnetization (under pulsed fields), and high-frequency/high-field ESR (HFESR) measurements. Also, we discuss the origin of the zero-field splitting parameter (D) of the ground states for **1**–**3** with the negative sign, which provides a base of the quantum tunneling of the magnetization (QTM).

EXPERIMENTAL SECTION

Synthesis. $[n\text{-}BuNH_3]_{12}[(CuCl)_6(SbW_9O_{33})_2]\cdot 6H_2O$ (**1**) was prepared according to the same procedure as $[n\text{-}BuNH_3]_{12}[(MnCl)_6(SbW_9O_{33})_2]\cdot 6H_2O$ (**3**) by use of $CuCl_2$ (1.0 g, 7.5 mmol) instead of $MnCl_2\cdot 4H_2O$ in water with a yield of 0.40 g in 65% based on W:[1] after filtration of an aqueous solution containing $Na_9[SbW_9O_{33}]\cdot 19.5H_2O$ (0.57 g, 0.2 mmol), $CuCl_2$ (1.0 g, 7.5 mmol), and n-$BuNH_3Cl$ (0.55 g, 5 mmol) in 30 mL of water, the clear filtrate was kept approximately for one week at room temperature (with slow evaporation of water), and orange crystals (0.31 g in 50% based on W) were isolated. Calcd: C, 9.30; H, 2.54; N, 2.71; Cu, 6.15; W, 53.37; Sb, 3.93%. Found: C, 9.08; H, 2.06; N, 2.70; Cu, 6.98; W, 52.8; Sb, 3.65%. IR (KBr disk) showed metal–oxygen stretches at $\bar{\nu}$ = 945 (m), 898 (m), 862 (m), 822 (s), 724 (s), 677 (s) cm^{-1}. Similarly, $(n\text{-}BuNH_3)_{12}[(MnCl)_6(AsW_9O_{33})_2]\cdot 6H_2O$ (**4**) was synthesized by the reaction between $Na_9[AsW_9O_{33}]\cdot 19.5H_2O$ and $MnCl_2\cdot 4H_2O$ in the presence of n-$BuNH_3Cl$:[1] after filtration of an aqueous solution containing $Na_9[AsW_9O_{33}]\cdot 19.5H_2O$ (0.57 g, 0.2 mmol), $MnCl_2\cdot 4H_2O$ (1.5 g, 7.5 mmol), and n-$BuNH_3Cl$ (0.55 g, 5 mmol) in 30 mL of water, the filtrate was kept approximately for one week at room temperature, and red crystals (0.39 g in 64% based on W) were isolated. Calcd: C, 9.52; H, 2.60; N, 2.78; Mn, 5.44; W, 54.65; As, 2.47%. Found: C, 9.35; H, 2.21; N, 2.74; Mn, 5.37; W, 54.9; As, 2.57%. IR (KBr disk) showed metal–oxygen stretches at $\bar{\nu}$ = 946 (m), 890 (m), 824 (s), 756 (s), 730 (s) cm^{-1}.

$(n\text{-}BuNH_3)_{12}[(CuCl)_6(AsW_9O_{33})_2]\cdot 6H_2O$ (**2**),[1] $(n\text{-}BuNH_3)_{12}[(MnCl)_6(SbW_9O_{33})_2]\cdot 6H_2O$ (**3**),[1] $Na_9[SbW_9O_{33}]\cdot 19.5H_2O$,[13] and $Na_9[AsW_9O_{33}]\cdot 19.5H_2O$[14] were synthesized by literature procedures. All other chemicals were of at least analytical grade and used without further purification.

X-ray Crystallography. Intensity data for the single crystal X-ray crystallography of **1** and **4** were measured on a Rigaku RAXIS-RAPID imaging plate diffractometer with graphite monochromatized Mo Kα (λ = 0.71069 Å) radiation at −100 °C in the same way as the cases of **2** and **3**.[1] Lorentz polarization effects and numerical absorption corrections (by using the following program: Numabs and Shape, T. Higashi, *Program for Absorption Correction*; Rigaku Corporation: Tokyo, 1999) were applied to the intensity data, and H atoms were not indicated in the calculation. All the calculations were performed using the CrystalStructure software package (*CrystalStructure 3.5.1:Crystal Structure Analysis Package*; Rigaku and Rigaku/MSC: 2000–2003).[15]

For **1** a total of 31290 reflections (ω scan and $2\theta_{max}$ = 55.0°) was collected, of which 4832 unique reflections (R_{int} = 0.042) were used. Crystal data: MW = 6200.59. Space group $R\bar{3}$ (No.148), a = 20.3753(1), c = 26.3587(3) Å, Z = 3, V = 9476.8(1) $Å^3$, ρ = 3.26 g cm^{-3}, μ = 179.5 cm^{-1}, $F(000)$ = 8442. Crystal size = 0.32 mm × 0.18 mm × 0.06 mm. Transmission factors of 0.04–0.34. The structure was solved by a direct method (SHELXS-97) and refined based on 3794 observed reflections (with $I > 3\sigma(I)$ and 185 parameters) to R_1 = 0.030 (refined against $|F|$) and R_w = 0.095 (refined against $|F^2|$). The highest residual electron density was 6.36 e $Å^{-3}$ at 0.64 Å from the O4 atom (the deepest hole was −1.73 e $Å^{-3}$ at 0.56 Å from the W1 atom). All the oxygen atoms were refined isotropically, due to the instability of their anisotropic refinement. All the metal (W, Sb, and Cu), Cl, and N atoms, and C1–C4 and C7–C8 atoms were refined anisotropically. Other atoms (O and C atoms) were refined isotropically, and site occupancies of C5, C6, C9, and C10 atoms were set to be $^1/_2$ through the refinement of their thermal parameters.

For **4** a total of 29640 reflections (ω scan and $2\theta_{max}$ = 55.0°) was collected, of which 4882 unique reflections (R_{int} = 0.054) were used. Crystal data: MW = 6055.29. Space group $R\bar{3}$ (No.148), a = 20.12(2), c = 27.43(3) Å, Z = 3, V = 9614(16) $Å^3$, ρ = 3.14 g cm^{-3}, μ = 173.9 cm^{-1}, $F(000)$ = 8262. Crystal size = 0.23 mm × 0.10 mm × 0.10 mm. Transmission factors of 0.02–0.18. The structure was solved by a direct method (SHELXS-97) and refined based on 4207 observed reflections (with $I > 1.0\sigma(I)$ and 245 parameters) to R_1 = 0.023 (refined against $|F|$) for $I > 2\sigma(I)$ and R_w = 0.051 (refined against $|F^2|$) for $I > 1.0\sigma(I)$. The highest residual electron density was 1.19 e $Å^{-3}$.

dx.doi.org/10.1021/ic202513q | *Inorg. Chem.* 2012, 51, 4606–4619

The site occupancies of two sets (C5 and C6; C9 and C10) of atoms were fixed at $^2/_3$ and $^1/_3$, respectively. All the atoms (except for disordered atoms) were refined anisotropically, and the disordered atoms were refined isotropically. All the metal (W, As, and Mn), Cl, O, and N atoms, and C1−C4 and C7−C8 atoms were refined anisotropically. Other C atoms, C5−C6 and C9−C10 atoms, were isotropically refined with their site occupancies of $^2/_3$ and $^1/_3$, respectively.

Further details on the crystal structure investigations may be obtained from the Cambridge Crystallographic Data Center (CCDC; e-mail, deposit@ccdc.cam.ac.uk) on quoting the depository numbers CCDC-299472 $[n\text{-BuNH}_3]_{12}[(\text{CuCl})_6(\text{SbW}_9\text{O}_{33})_2]\cdot 6\text{H}_2\text{O}$ (CuSb) and CCDC-299473 $[n\text{-BuNH}_3]_{12}[(\text{MnCl})_6(\text{AsW}_9\text{O}_{33})_2]\cdot 6\text{H}_2\text{O}$ (MnAs).

Physical Measurements. IR (as KBr pellet) and UV/vis spectra were recorded on Jasco FT-IR 5000 and Jasco V-570 UV−vis−NIR spectrometers, respectively. The contents of As, Sb, Cu, Mn, and W were determined by X-ray fluororescence analysis on a Shimadzu EDX-800 spectrometer. The water content was measured by a thermogravimetric method on an ULVAC-TGD9600MTS9000 instrument. The magnetic susceptibility in the range 1.8−300 K was measured with a Quantum Design MPMS-XL5 SQUID magnetometer, and the experimental data were corrected for the contribution of the sample holder and for the diamagnetism of the sample estimated from Pascal's constants.[16] X-band ESR measurements were carried out on a JEOL ESR spectrometer (JES-RE1X) equipped with an Oxford Instruments cryostat (ESR 910). The standard inductive method was employed for magnetization measurements using a pulsed magnetic field at Tohoku University, and fast pulsed magnetic fields up to 10^3 T/s were generated by a capacitor bank of 90 kJ, as described elsewhere.[3,4,17] The sample was immersed in liquid ^{3}He to reach a temperature as low as 0.5 K. High-frequency ESR (HFESR) studies on crystalline were performed in the 54−190 GHz frequency range on a homemade spectrometer at Inst. Mater. Res., Tohoku University, where Gunn diodes were used as light sources for the high frequency in the measurements under the high magnetic fields.

RESULTS

Structure. The structures of **1** and **4** are similar to those of **2** and **3** respectively reported previously by us, since As^{III} (Sb^{III}) in **2** (**3**) coming from $[\text{AsW}_9\text{O}_{33}]^{9-}$ ($[\text{SbW}_9\text{O}_{33}]^{9-}$) has now been replaced by Sb^{III} (As^{III}) coming from $[\text{SbW}_9\text{O}_{33}]^{9-}$ ($[\text{AsW}_9\text{O}_{33}]^{9-}$). Because of this similarity, we will not proceed to the full description of its structure. **1**−**4** crystallize in the $R\bar{3}$ space group, and $[(\text{MCl})_6(\text{XW}_9\text{O}_{33})_2]^{12-}$ (M = Cu^{II} and Mn^{II}; X = Sb^{III} and As^{III}) as an anion consists of a M_6 hexagon ring sandwiched by two α-B-$[\text{XW}_9\text{O}_{33}]^{9-}$ ligands with the D_{3d} symmetry linkage, each of which bridges six M atoms in a $\mu_6{:}\eta^2{:}\eta^2{:}\eta^2{:}\eta^2{:}\eta^2{:}\eta^2$ fashion through M−O−M bonds by six μ_3-O atoms. The anion charges are neutralized by 12 $[n\text{-BuNH}_3]^+$ cations around the anion.

Figure 1 exemplifies the structures of anion (a) and Cu_6 hexagon consisting of six edge-shared $\text{ClCu}(\mu_3\text{-O})_4$ square pyramids (b) for **1**. The M atom is coordinated by four μ_3-O atoms (with M−O distances 1.98−2.00, 1.97−1.99, 2.10−2.13, and 2.12−2.13 Å for **1**−**4**, respectively) belonging to two B-α-$[\text{XW}_9\text{O}_{33}]^{9-}$ ligands and an exterior Cl atom (with M−Cl distances 2.47, 2.49, 2.39, and 2.40 Å for **1**−**4**, respectively) in a square pyramidal geometry and is positioned at 0.43, 0.40, 0.67, and 0.63 Å for **1**−**4**, respectively, above the four μ_3-O atoms least-squares plane. Six M atoms make an equatorial hexagon ring (with a first-neighboring M···M distance of 2.94, 2.91, 3.25, and 3.23 Å, a M−O−M bond angle of 95, 95, 100, and 99°, and second- and third-neighboring M···M distances of 5.09 and 5.88, 5.05 and 5.83, 5.63 and 6.50, and 5.59 and 6.46 Å for **1**−**4**, respectively, with the neighboring M−M−M angle of 120°). The M_6 hexagon skeleton consists of six edge-sharing ClMO_4 square pyramids with a dihedral angle of 120° between neighboring

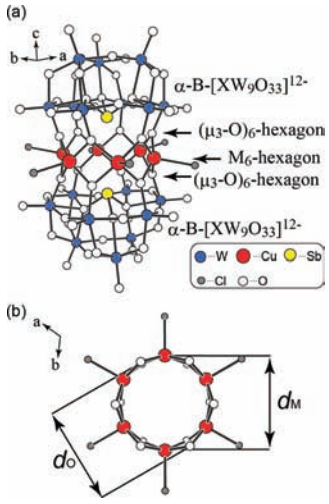

Figure 1. Molecular structures of anion (a) and Cu_6 hexagon consisting of six edge-shared $\text{ClCu}(\mu_3\text{-O})_4$ square pyramids (b) for **1**. Diameters (d_{M} and d_{O}) of Cu_6 and $(\mu_3\text{-O})_6$ hexagon rings correspond to third-neighboring Cu···Cu and $\text{O}(\mu_3)\cdots\text{O}(\mu_3)$ distances, respectively.

least-squares $(\mu_3\text{-O})_4$ planes, and it involves two $(\mu_3\text{-O})_6$ hexagon rings (with diameters of 5.79, 5.81, 5.94, and 5.99 Å for **1**−**4**, respectively) above and below the M_6 hexagon ring (with diameters of 5.88, 5.83, 6.50, and 6.46 Å for **1**−**4**, respectively). Six atoms in each of the M_6 and $(\mu_3\text{-O})_6$ hexagon rings adopt a coplanar conformation, and the least-squares plane of the M_6 hexagon ring is positioned at a symmetrical distance from the two X atoms at the X···X distances 4.81, 5.28, 4.94, and 5.40 Å for **1**−**4**, respectively, along with the *c*-axis in the unit cell. Short Sb···Sb distances (for **1** and **3**) compared to the As···As distances (for **2** and **4**) arise from longer Sb−O distances (1.96 Å) compared to As−O distances (1.79 Å), as reflected by the fact that the O−Sb−O angles (91−92°) are smaller than the O−As−O angles (97° for **2** and **4**) for the XO_3 trigonal pyramid in the B-α-$[\text{XW}_9\text{O}_{33}]^{9-}$ ligand. The six M atoms cap the hexagonal prism constructed by 12 μ_3-O atoms from two $(\mu_3\text{-O})_6$ hexagons to give a $\text{M}_6(\mu_3\text{-O})_{12}$ hexacapped-hexagonal-prismatic geometry. Table 1 lists selected interatomic distances (in Å) and angles (deg) for anions in **1**−**4** for comparison. The most salient feature of the comparative structures for **1**−**4** is that the diameter (5.83 Å) of the Cu_6 hexagon ring in **2** is very close to the one (5.81 Å) of the $(\mu_3\text{-O})_6$ hexagon ring to provide a $\text{Cu}_6(\mu_3\text{-O})_{12}$ cylindrical geometry, while the diameter (5.88, 6.50, and 6.46 Å) of the Cu_6 (or Mn_6) hexagon ring for others (**1**, **3**, and **4**) is larger than the one (5.79, 5.94, and 5.99 Å) of the $(\mu_3\text{-O})_6$ hexagon ring. In particular, the Mn_6 hexagon ring diameter is much larger (6.5 Å) than the $(\mu_3\text{-O})_6$ hexagon ring diameter (5.9−6.0 Å), indicating a large deviation of Mn atoms from the cylindrical geometry of two $(\mu_3\text{-O})_6$ hexagon rings.

dc Magnetic Susceptibility Studies. The variable-temperature (T) molar susceptibility (χ_{M}) studies were performed on the polycrystalline samples. Figure 2 shows Curie−Weiss plots of χ_{M}^{-1} vs T under the 0.1 T field for **1**−**4**. The linear relationship of χ_{M}^{-1} and T at the range more than 150, 100, 50, and 2 K shows the Weiss constants (θ) of +45.5, +28.7, +8.6, and −2.5 K for **1**−**4** respectively indicative short-range ferromagnetic coupling for **1**−**3** (Figure 2a−c) and antiferromagnetic coupling for **4** (Figure 2d). The Curie constants (C) of 2.78, 2.91, 26.2, and 23.1 emu·K·mol^{-1} for **1**−**4** are related to the effective

dx.doi.org/10.1021/ic202513q | Inorg. Chem. 2012, 51, 4606−4619

Table 1. Interatomic and Atom/Plane Distances (Å) and O−X−O and M−O−M Bond Angles (deg) for $[(MCl)_6(XW_9O_{33})_2]^{12-}$ (M = Cu^{II} and Mn^{II}; X = As^{III} and Sb^{III}) in 1−4 at −100 °C

	1	2 (ref 1)	3 (ref 1)	4
M−O(μ_3)	1.977(7), 1.991(7)	1.991(6), 1.976(5)	2.121(5), 2.126(4)	2.129(5), 2.123(6)
	1.991(7), 1.997(7)	1.972(6), 1.968(7)	2.101(4), 2.126(4)	2.123(4), 2.122(5)
M−Cl	2.467(4)	2.490(3)	2.391(3)	2.395(3)
W−O(μ_3)	1.865(8), 1.864(8)	1.866(5)	1.851(5)	1.835(5), 1.834(5)
M···M[a]	2.938(1)	2.913(2)	3.248(1)	3.228(2)
	5.088(2)	5.045(2)	5.625(1)	5.590(2)
	5.876(2)	5.825(2)	6.495(2)	6.455(2)
O(μ_3)···O(μ_3)[b]	5.79(1)	5.812(9)	5.942(8)	5.99(1)
X···X	4.813(2)	5.278(2)	4.943(1)	5.408(2)
X−O	1.959(8)	1.786(6)	1.964(5)	1.791(6)
O−X−O	91.0(3)	96.8(2)	92.2(2)	96.9(3)
M−O(μ_3)−M	94.9(3), 95.5(3)	95.3(2), 94.52(2)	100.4(2), 99.8(2)	99.0(2), 98.8(2)
M···[c] (μ_3-O)$_4$ square-plane	0.432	0.396	0.674	0.634
O(μ_3)···[d] M_2W triangle plane	0.032, 0.105	0.009, 0.065	0.106, 0.201	0.081, 0.160

[a]First-, second-, and third-neighboring M···M distances for the equatorial M_6 hexagon ring with the neighboring M−M−M angle of 120°. The third-neighboring M···M distance corresponds to the M_6 hexagon ring diameter. [b]Third-neighboring O···O distance for the (μ_3-O)$_6$ hexagon ring, which corresponds to its ring diameter. [c]Location of the M atom from the least-squares (μ_3-O)$_4$ plane in the $ClMO_4$ square pyramid. [d]Location of the μ_3-O atom from the M_2W-triangle plane.

magnetic moment (μ_{eff}) of 4.71, 4.82, 14.5, and 13.6 Bohr magnetons (μ_B) according to C (in $cm^3 \cdot mol^{-1}$) = 0.1251 μ_{eff}^2, which are close to the sum of spin-only contributions of 6 Cu^{2+} (4.24 μ_B) or 6 Mn^{2+} (14.5 μ_B) with g = 2, respectively. The data at the range 1.8−300 K for **1** (a) and **4** (b) are analyzed by plotting $\chi_M T$ vs T at 0.1 T, as shown in Figure 3, where the field-dependent magnetizations (M) in μ_B per mole unit in the applied dc fields (B) at 1.8 K are also added. The values of $\chi_M T$ at 0.1 T slowly increase from ca. 3.3 emu·K·mol^{-1} (corresponding to ca. 5.1 μ_B) at 300 K to a maximum (9.1 emu·K·mol^{-1}) around 7 K and then decrease to ca. 6−7 emu·K·mol^{-1} at 1.8 K. The maximum $\chi_M T$ value for **1** is slightly higher than the saturation value (6.00 emu·K·mol^{-1}) for the spin only (g = 2) isolated S = 3 ground state. The behavior of the plots of $\chi_M T$ vs T for **2** was similar to the one for **1**, as was previously shown.[1] The $\chi_M T$ value for **4** shows 23 emu·K·mol^{-1} (corresponding to ca. 13.6 μ_B) at 300 K and steeply decreases from 21 emu·K·mol^{-1} around 30 K to 8.6 emu·K·mol^{-1} at 1.8 K (Figure 3b). This behavior for **4** is in strong contrast with the behavior for **3**, which slowly increased from 27 emu·K·mol^{-1} (corresponding to ca. 14.7 μ_B) at 300 K to 32 emu·K·mol^{-1} (corresponding to ca. 16.0 μ_B) at 30 K and sharply increased to a maximum of 106 emu·K·mol^{-1} (corresponding to ca. 29.1 μ_B) at 2 K with a slight decrease of 99 emu·K·mol^{-1} at 1.8 K, as was previously shown.[1] As shown in the inset of Figure 3a, the M value for **1** increases with increasing B values with an approximately linear relationship at ≤0.5 T, and it reaches a plateau of approximate 6 μ_B, which is close to the magnetization value of the S = 3 ground state. On the other hand, the magnetization of the antiferromagnetic **4** increases with the approximately linear relationship up to a maximum field of 5 T to yield 22 μ_B even in 5 T (inset of Figure 3b), suggesting that the magnetization is through the crossover among the S = 0 ground state and the excited states due to the usual Zeeman interaction.

Figure 4 shows the zero-field-cooled (ZFC) and field-cooled (FC) magnetism measurements of the dc magnetic susceptibility,

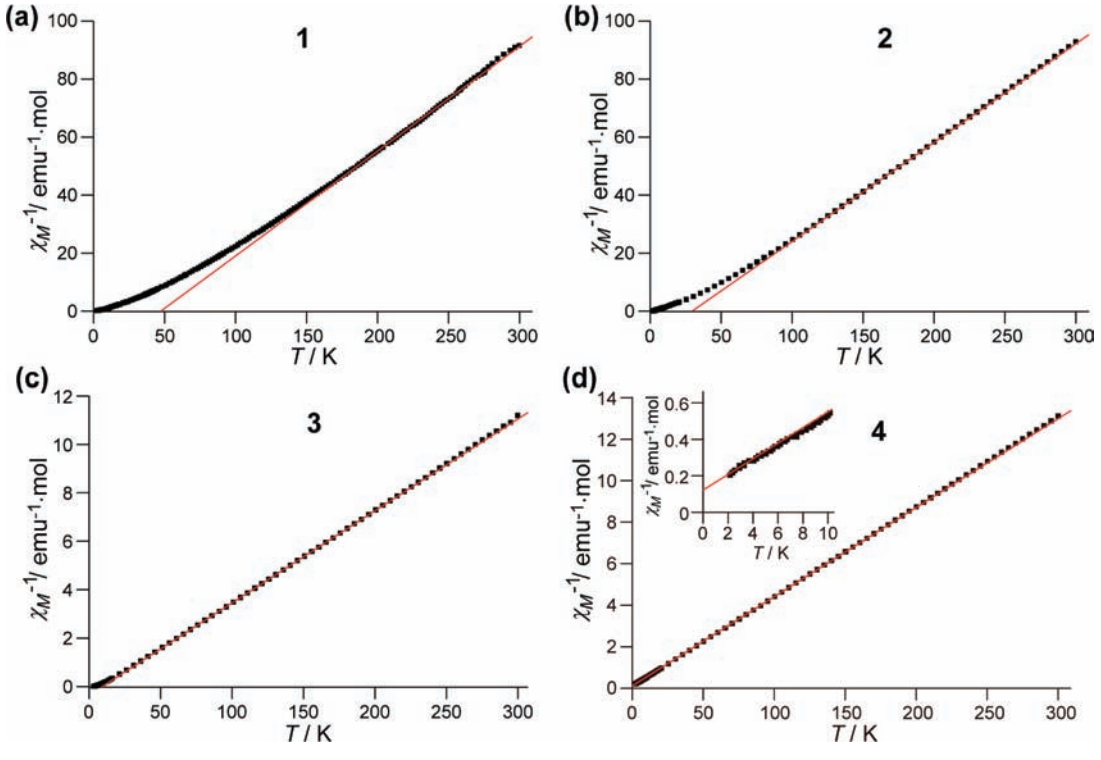

Figure 2. Curie−Weiss plots of χ_M^{-1} vs T under the 0.1 T field for **1**−**4**. The inset in part d shows an expansion of the 2−10 K region, with the solid red line a fit to a Curie−Weiss law.

dx.doi.org/10.1021/ic202513q | Inorg. Chem. 2012, 51, 4606−4619

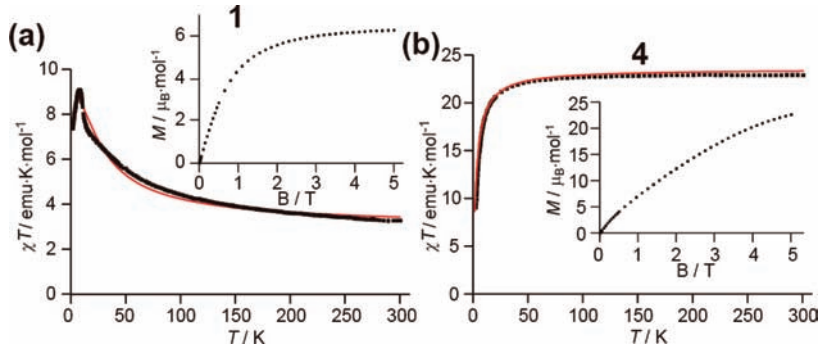

Figure 3. Plots of $\chi_M T$ vs T at the range 1.8−300 K under 0.1 T for **1** (a) and **4** (b). Inset figures indicate field-dependent magnetizations (M) in μ_B per mole unit under dc fields (B) at 1.8 K. The best-fit red lines (obtained using parameter values given in the text) for **1** and **4** are shown for 7−300 K and 1.8−300 K, respectively.

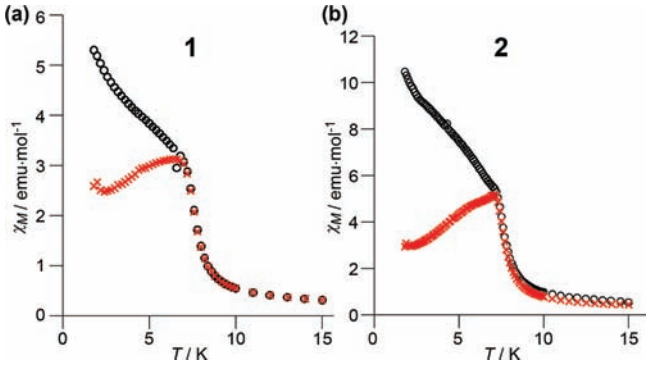

Figure 4. Plots of zero-field-cooled (ZFC) and field-cooled (FC) magnetization vs T for **1** (a) and **2** (b). Red crosses and black open circles indicate plots of ZFC and FC magnetization, respectively.

χ_{ZFC} and χ_{FC}, for **1** and **2**. If the samples are cooled down to 1.8 K in zero field, a low signal appears as a consequence of the absence of a preferential orientation of the magnetic domains in the weak ferromagnet. When warming the samples in the presence of a dc magnetic field of 5 Oe, the susceptibility increases due to the progressive orientation of the domains and reaches a maximum centered at approximately 7 K. Above this temperature, the magnetic susceptibility is typical of a paramagnet. Thus, the field cooled susceptibility curves for **1** and **2** diverge from the ZFC ones below approximately 7 K as the bifurcation (ordering) temperature (T_b) due to the formation of magnetic domains aligns with the applied dc field, suggesting the presence of a remnant magnetization below T_b, which increases upon cooling. The samples of **3** and **4** did not exhibit such bifurcation temperature arising from the irreversibility at $T \geq$ 1.8 K. To get more information about the long-range magnetic ordered state and the ordering temperature for ferromagnetic samples of **1**−**3**, ac susceptibility measurements in the temperature range 1.8−10 K at different ac frequencies in the 0.1−1200 Hz range have been performed. Figure 5 shows the temperature dependences of the in-phase χ_M' and the out-of-phase χ_M'' components of the ac susceptibility in a 3.6 Oe oscillating magnetic field. As shown in Figure 5, the ordering temperatures at which χ_M'' becomes nonzero are 7.5, 7.3, and 3.0 K for **1**−**3**, respectively. The frequency-dependent χ_M'' signals indicate the magnetization relaxation relative to the frequency of the oscillating ac field. The full peak observed for **1** and **2** is shifted slightly toward lower temperatures as the frequency of the oscillating field decreases, and for **3** the peaks appearing at high

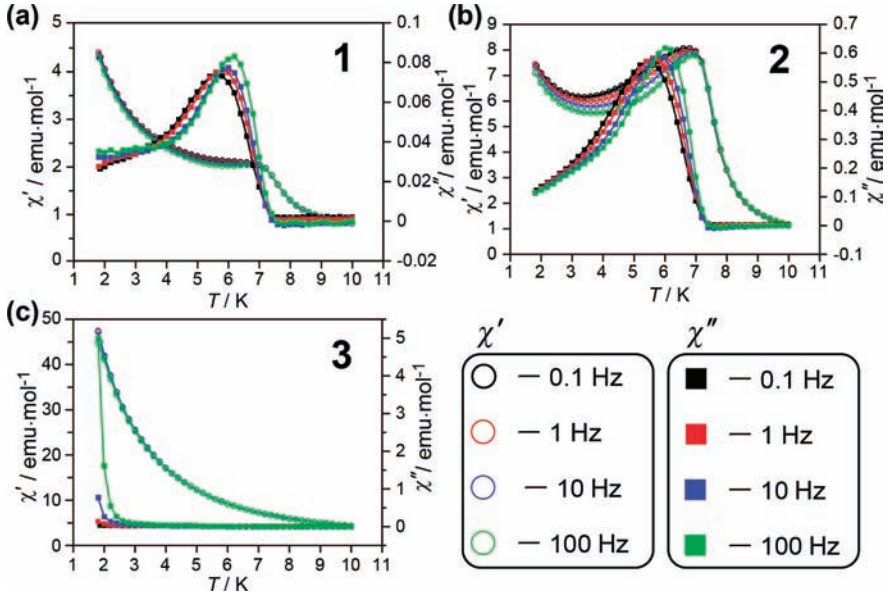

Figure 5. Temperature dependences of the in-phase χ_M' and out-of-phase χ_M'' components of ac susceptibility at four characteristic frequencies for **1**−**3**, measured in a 3.6 Oe oscillating magnetic field.

dx.doi.org/10.1021/ic202513q | Inorg. Chem. 2012, 51, 4606−4619

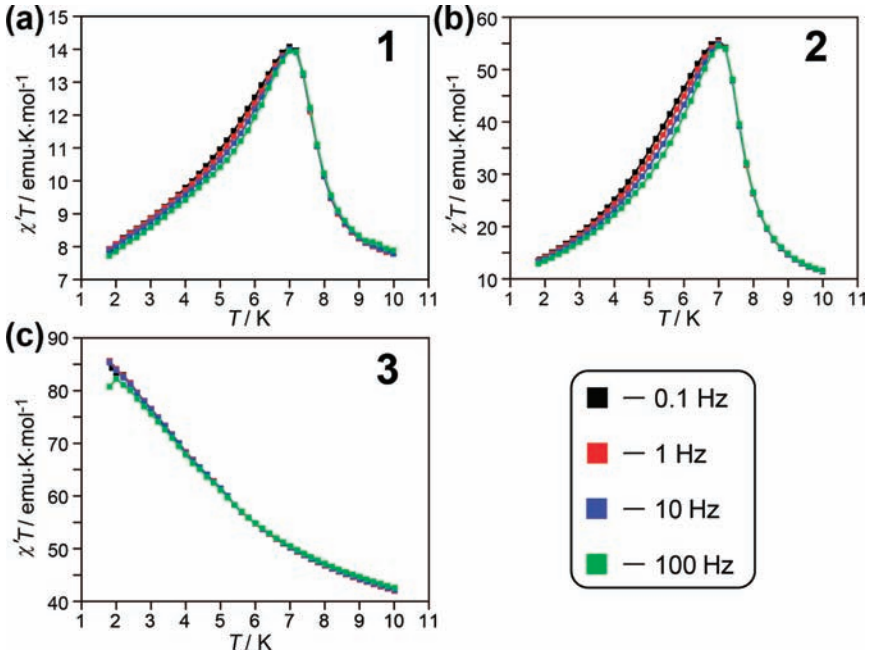

Figure 6. Plots of $\chi_M'T$ vs T, measured in a 3.6 Oe oscillating magnetic field.

frequencies (>500 Hz) seem to disappear at low frequencies (≤200 Hz) to be shifted to the temperature of T < 1.8 K of the measured lowest temperature. While the $\chi_M'-T$ plots for **1**−**3** show shoulder-like peaks of Figure 5, the $\chi_M'T-T$ plots show distinct peaks of $\chi_M'T$ values, as shown in Figure 6, where the $\chi_M'T$ values at T < 10 K increase with decreasing temperature, irrespective of the change of frequency, and frequency-dependently decrease through a maximum at ca. 7 K for **1** and **2** and ca. 2 K for **3**. The $\chi_M'T$ values at less than 10 Hz were least-squares fit and then extrapolated to 0 K to estimate the ground-state spins of molecules, to avoid the possible Zeeman effect.[18] The values taken from 1.8 to 7 K for **1** and **2** were extrapolated to 0 K, to give $\chi_M'T$ = 6.4 and 6.7 emu·K·mol^{-1}, respectively, which correspond to the S = 3 ground state predicted by the spin-only formula for **1** and **2**. The extrapolation to 0 K for **3** was not done due to the ambiguity of the low-temperature $\chi_M'T$ values measured at the range of temperatures higher than 1.8 K.

Magnetization under Pulsed Field. The measurement of the magnetization behavior of **1**−**4** under the adiabatic condition at the lowest temperature was done by using the pulsed magnetic field, which takes either a half-sine wave shape or a full cycle.[17] Figure 7 shows the magnetizations of **1**−**4** under a half cycle (for **1**) and a full-cycle (for **2**−**4**) of the pulsed field waveform at 0.5 K. The inset in Figure 7b shows the pulse-field waveform of the full cycle. The field sweep rate is not constant in the pulsed magnetic field: for the half-cycle the up-sweep rate is as high as approximately 10^3 T/s at the starting point (B = 0) but decreases to zero at the maximum of B, and thereafter, the down-sweep rate increases up to approximately 10^3 T/s around the end (B = 0). For the full-cycle the down-sweep rate from B = 0 decreases to zero at the minimum of B from approximately 10^3 T/s at the starting point, and thereafter, the up-sweep rate increases to approximately 10^3 T/s again around B = 0. The experimental curves of **1**−**3** under the pulse field (in both the half cycle and the full cycle) deviate from the Brillouin-functioned magnetization curves under the steady field (inset in Figure 3a), indicating a hysteresis due to

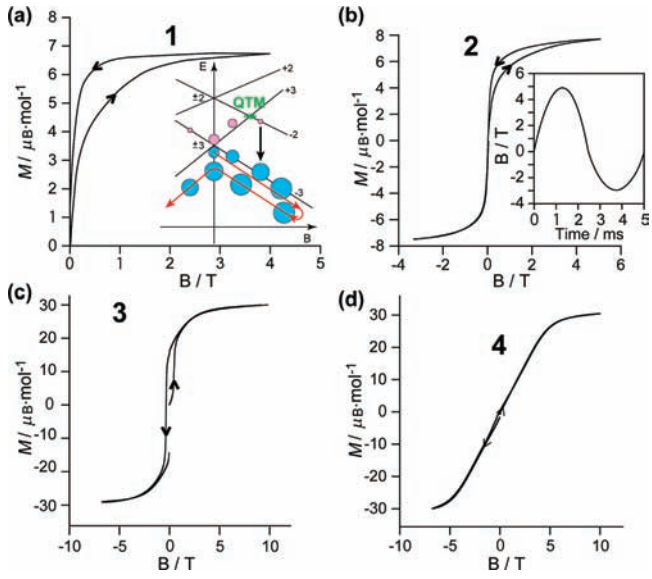

Figure 7. Magnetization curves vs pulsed magnetic field at 0.5 K for polycrystalline samples of **1**−**4**. The inset of Figure 7a schematically illustrates variation of spin populations at the m_s = ±3 sublevels (+3 by pink filled circles and −3 by blue filled circles) for the S = 3 ground state on the up- and down-sweeps (indicated by red arrow) of the pulse-field together with the Zeeman splitting energy variation of m_s = ±3 and m_s = ±2 sublevels in D < 0, when the field is parallel to the easy axis. The green and black arrows denote the quantum tunneling at the S_z = +3 → S_z = −2 Zeeman crossover and the Δm_s = ±1 allowed S_z = −2 → S_z = −3 relaxation, respectively. The inset of Figure 7b exemplifies the waveform of the pulsed magnetic field (B) versus time for a full cycle.

the nonequilibrium of the magnetization. When the field from B = 0 increases, the magnetization rapidly increases at B < 1 T and gradually approaches saturation around 6 μ_B (for **1** and **2** above ~3 T) and 30 μ_B (for **3** above ~5 T). In the down sweep from the highest field the magnetization gradually decreases, being higher than that in the first quarter cycle. Such hysteresis

dx.doi.org/10.1021/ic202513q | Inorg. Chem. 2012, 51, 4606−4619

is understood by considering the competition between the thermal relaxation and the fast change of the magnetic field. The hysteresis in the first half cycle leads to a sharp reversal around $B = 0$ under the next quarter cycle followed by a minor hysteresis in the negative field through a full cycle (Figures 7b and c), supporting the ferromagnetic interaction. The sharp reversal magnetization indicates the negative sign of the zero-field splitting (ZFS) parameter (D) for the ground states of **1**−**3**, if a simple Zeeman crossing at $B = 0$ for the ground state ($S = 3$ for **1** and **2** and $S = 15$ for **3**) is assumed. It is notable for **3** to exhibit the hysteretic behavior with a coercive field of approximately 0.5 T and a remnant magnetization of 15 μ_B (=28 emu·K·mol^{-1}) at 0.5 K (Figure 7c). In contrast, the magnetization of **4** is not hysteretic and is similar to the magnetization curves under the steady field (inset in Figure 3a): it approximately linearly increases with an increase of the pulse field at $B < 5$ T, and it reaches the saturation value of ∼30 μ_B in higher positive fields above ∼7 T (Figure 7d). Together with the nonhysteretic reversal magnetization in the negative field through the second half cycle, the magnetization behavior supports the antiferromagnetic interaction for **4** (with the $S = 0$ ground state at $B = 0$).

To explain the magnetization of **1** and **2** under the pulsed field, the inset of Figure 7a presents a schematic view of energy levels under the Zeeman effect in which the Zeeman splitting of $S_z = \pm m_s$ ($m_s = 3, 2, 1, 0$ for **1** and **2**) sublevels at $D < 0$ is denoted by using the notation of $S_z = -m_s$ and $S_z = +m_s$ as quantum numbers of the projection of the spin angular momentum onto the applied magnetic field axis. The spin population for two sublevels of $m_s = \pm 3$ changes from approximate equality at $B = 0$ before the pulse in the positive side of the magnetic field, since $S_z = -3$ and $S_z = +3$ are the ground and excited states, respectively. The equilibrium value of the population in the two sublevels is given by the partition function with parameters of both temperature and magnetic field intensity. If the magnetic field is swept from zero to the positive finite value and the sweep time is much longer than the relaxation time between the two sublevels, the magnetization should take the equilibrium value given by the Brillouin function. When the sweep rate is fast enough to achieve the nonequilibrium, however, no relaxation occurs and the initial equal population must be kept with a resultant zero magnetization due to the cancellation of each magnetization of the spins in the two sublevels $S_z = -3$ and $S_z = +3$. When the relaxation time is much longer than the time period of the field sweep (which is proportional to the inverse of the filed sweep rate), therefore, the small and gradual increase of the magnetization under the first quarter cycle of the pulse field results from the $\Delta m_s = \pm 1$ allowed $S_z = -2 \rightarrow S_z = -3$ relaxation through the $S_z = +3 \rightarrow S_z = -2$ Zeeman crossover (possibly by the quantum tunneling). Since the sweep rate reaches zero at the maximum field (4−5 T), thus, the relaxation comes into effect around this field. In the down sweep after the maximum, the magnetization (at the $S_z = -3$ ground state under the positive field) remains nearly constant due to the high population of the spin at the ground state, which leads to the rapid reversal (to the $S_z = +3$ ground state under the negative field) through the $S_z = -3 \rightarrow S_z = +3$ Zeeman crossover (possibly also by the quantum tunneling) at $B = 0$ with quenching of the thermal relaxation in the fast sweep rate of the magnetic field. The minor hysteresis in the negative field side can be understood by the high population of the $S_z = +3$ ground state in the second half cycle. Since the thermal relaxation from $S_z = +3$ to $S_z = -3$ is the parity-forbidden transition and would be almost inhibited at the fast sweep rate during the second half cycle, the observation of the rapid reversal magnetization around $B = 0$ (Figure 7b) results from the quantum tunneling of the magnetization (QTM) at $B = 0$. If there is no QTM, the magnetization should be positive even in the negative field side: the sharp reversal is not expressed by the Brillouin curve, which can be applied only for the equilibrium magnetization process.

Figure 8 shows the differential magnetization (dM/dB) plots against the pulsed field for better understanding of the magnetic hysteresis of **1**−**3** at 0.5 K. The dM/dB plots under the half cycle in the range 0−0.7 T show several distinct peaks, at least three peaks around 0.07, 0.13, and 0.20 T for **1** (Figure 8a) and around 0.15, 0.23, and 0.28 T for **2** (Figure 8b), and the field dependence of dM/dB around $B = 0$ for **2** displays a broadened peak at $B = 0$ (inset in Figure 8b). The dM/dB plot

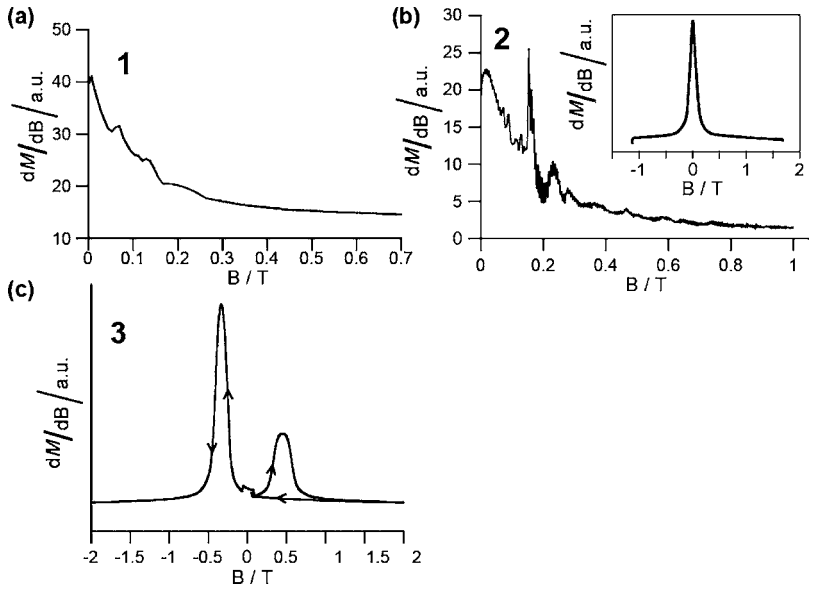

Figure 8. Differential magnetization (dM/dB) plots against the pulsed field for **1**−**3** at 0.5 K.

dx.doi.org/10.1021/ic202513q | Inorg. Chem. 2012, 51, 4606−4619

in the range ±2 T for **3** shows a peak at 0.47 T on the up sweep from B = 0 and a broad peak at −0.33 T on the down sweep from B = 2 T (Figure 8c). Since the peak in dM/dB corresponds to the step in the magnetization, the change of magnetization in the adiabatic process reveals QTM at the Zeeman crossed fields which may be used for estimation of the magnitude of the axial ZFS parameter D. A strong peak at B = −0.33 T (not at B = 0) on the down sweep from B = 2 T for **3** may be understood by both the coercive field of approximately 0.5 T and the remnant magnetization of 15 μ_B at B = 0, which imply a still large population of spins at the S_z = −15 level under the negative field around B = 0 (Figure 7c). The QTM resonances observed in the hysteresis measurements for **1**−**3** will be again discussed below in conjunction with the magnitude of D.

ESR Spectroscopy. To obtain an independent assessment of g and D, high-frequency/high-field ESR (HFESR) measurements are performed on a portion of the same polycrystalline samples used for the above magnetic susceptibility studies. In principle, both the ground state spin (S) and the ZFS parameter D can be determined directly via HFESR experiments. In particular, the D parameter splits the ESR spectrum into 2S fine structure peaks whose spacing depends on the magnitude of D and the orientation of the applied field relative to the easy-axis (z) of the sample; in the true high-field limit ($g\mu_B B \gg |DS|$), the spacing in the field is $2|D|/g\mu_B$ and $|D|/g\mu_B$ for the applied field, B, parallel and perpendicular, respectively, to the z-axis. For the case of a powder sample having a significant S, one may expect to see a splitting in the ESR pattern at low temperatures because of the extrema of the parallel (z) and perpendicular (xy) components of the spectrum. Thus, it is only possible to estimate the product DS in this case. Furthermore, from the temperature dependence of the ESR spectrum pattern, one expects independently to verify the sign of D, which is achieved from the above magnetization data under a pulse field. Since the presence of the C_3 crystal site symmetry in D_{3d}-spin hexagons of **1**−**3** would preclude the rhombic ZFS term of $E(\hat{S}_x^2 - \hat{S}_y^2)$, we assume that the Hamiltonian system is simplified as the axially symmetric system as followed by eq 1,

$$\hat{H} = \mu_B \hat{S} g B + D\hat{S}_z^2 \quad (1)$$

where $\hat{S}_z$ is the operator for the component of the spin vector along the z-axis, and other symbols have their usual meaning. This Hamiltonian assumes that only the ground state (S = 3 for **1** and **2**, and S = 15 for **3**) is populated at these temperatures and magnetic fields and includes isotropic Zeeman interactions and axial ($D\hat{S}_z^2$) ZFS. It is clear that both space groups of $R\bar{3}$(No.148) and Z = 3 for the crystals show that all patterns of the HFESR spectra result from a crystallographically single independent Cu_6 hexagon site in the unit cell.

Figure 9 shows HFESR spectra for **1** (a) and **2** (b) at 190 GHz and in a range of temperatures between 4.2 and 50 K. The figures display the signal transmitted through the cavity, and the dips in transmission consequently correspond to absorption within the cavity. The spectra of **2** exhibit considerable asymmetry and line broadening that increase for transitions occurring at higher fields when compared with those of **1**. At the lowest temperature (4.2 K), significant populations exist at the ground and first excited m_s sublevels as a result of ZFS. As the temperature increases, the spectral weight (of four lines around 5.2, 5.5, 5.8, and 6.0 T) shifts toward transitions occurring at higher magnetic fields. The shifting pattern is in accord with the pattern expected for a system with a negative D value, if the lines are assigned to the transitions obtained with the field close to the easy z axis. Arrows depicted in Figure 9 indicate the peak assignments of four Δm_s= ±1 allowed $m_s \rightarrow m_{s+1}$ transitions. In the low-temperature limit where the spectral weight shifts to low fields, a relatively intensive line

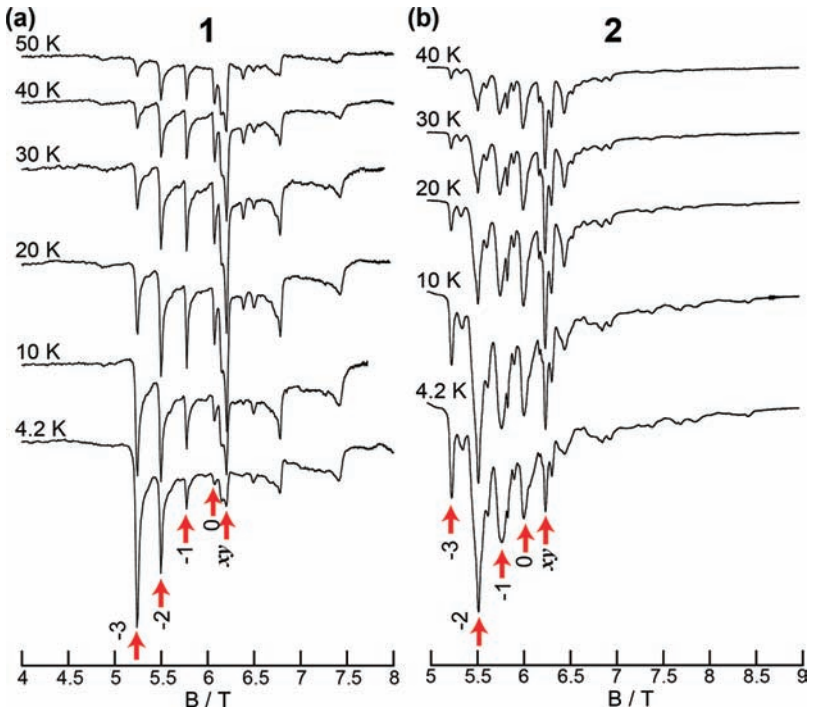

Figure 9. High-field ESR (HFESR) spectra for **1** (a) and **2** (b) at 190 GHz and in a range of temperatures between 4.2 and 50 K. Red arrows (by −3, −2, −1, 0, and xy) indicate four Δm_s = ±1 allowed $m_s \rightarrow m_{s+1}$ easy-axis lines (−3 → −2, −2 → −1, −1 → 0, and 0 → +1) and the distinguished hard (xy)-axis line, respectively.

dx.doi.org/10.1021/ic202513q | Inorg. Chem. 2012, 51, 4606−4619

around 6.3 T at 4.2 K for **1** and **2** is distinguishable from the above easy-axis lines. This can be related with the one of the transitions obtained with the field in the hard (xy) plane. The powder HFESR spectra of **1** and **2** are contaminated by many other peaks at B > 6.5 T. Nevertheless, the first five stronger easy-axis and hard plane peaks can be clearly identified. Thus, we can estimate $g_{\|}$, $g_{\perp}$, and D for the S = 3 ground state from slope and zero-field offset on the plot of the $\Delta m_s = \pm 1$ resonance positions for the two orientations at various frequencies. The linear plot lines produce slopes (33.3 and 32.0 GHz/T for the easy-axis and 30.7 and 30.0 GHz/T for the hard-plane) and zero-field offsets (20.0 and 21.5 GHz) in the situation of the lowest-field easy-axis line for **1** and **2**, respectively. Figure 10 exemplifies the frequency-dependence

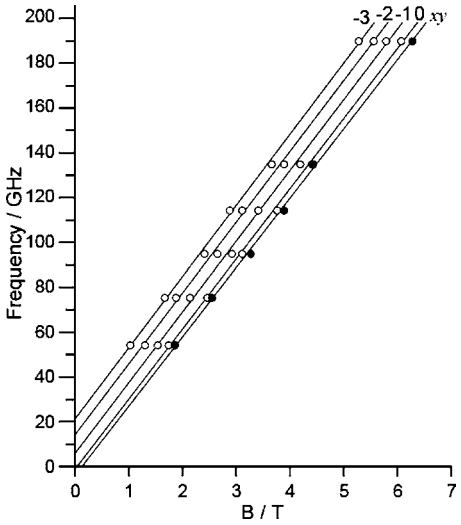

Figure 10. Frequency-dependence of five HFESR transition peaks occurring at lower fields for **2** between 54.3 and 190 GHz with the field close to the easy axis (open circles) and aligned in the hard plane (filled circle) at 20 K. The solid lines are the fits of the data, from which the Hamiltonian parameters given in the text were obtained.

for **2** between 54.3 and 190 GHz with the field close to the easy axis and aligned in the hard plane at 20 K. Since the zero-field offset value obtained from the linear plot for the lowest-field peak of the easy-axis corresponds to $(3^2 - 2^2)|D|$, thus, the linear plots for the easy axis and the hard plane give the Hamiltonian parameters (eq 1) and represent D = −0.147 cm^{-1}, $g_{\|}$ = 2.30, and $g_{\perp}$ = 2.19 for **1** and D = −0.145 cm^{-1}, $g_{\|}$ = 2.29, and $g_{\perp}$ = 2.14 for **2**. The set of parameter values for **2** gives a good agreement with the one ($g_{\|}$ = 2.22 and D = −0.127 cm^{-1}) estimated from the 190-GHz single crystal HFESR spectrum in the easy-axis orientation.[1]

Figure 11 shows the powder HFESR spectra (a) collected over the temperature range 4.2−30 K at 135 GHz and the frequency-dependence diagram (b) for the easy-axis orientation at 4.2 K between 81.5 and 190 GHz for **3**. In the powder HFESR patterns of **3**, a particularly notable feature of the patterns in accordance with D < 0 is the fact that the easy-axis peaks seen at higher field under the lowest temperature are sharp enough to estimate $g_{\|}$ and D values, in contrast with the case of **4** (Supporting Information Figure S1), which showed no fine-structural magnetic-dipole transition lines for the low-lying spin-multiples. As shown in Figure 11b, the frequency-field diagram for the easy-axis orientation indicates the linear dependence and the linear plot for the lowest-field peaks shows a gap of 67 GHz (the offset for the signal of the energy gap of $(15^2-14^2)|D|$ at zero field between the m_S = −15 ground-state and the m_S = −14 first-excited-state levels), if one assumes the lowest lying spin multiplet of S = 15. This gives $g_{\|}$ = 2.03 and D = −0.077 cm^{-1} for **3**.

Estimation of Magnetic Exchange Interactions. For determination of the exchange interactions within each Cu_6 or Mn_6 hexagon of **1**−**4**, at first, the $\chi_M T$ vs T data were fit to the spin exchange Hamiltonian ($\hat{H}_{exchange}$) given by eq 2. Assuming only nearest neighbor interactions $\hat{H}_{exchange}$ of a ring of approximately equilateral Cu_6 or Mn_6 hexagon for **1**−**4** with a cyclic boundary condition, $S_{6+1} = S_1$ takes the form

$$\hat{H}_{\text{exchange}} = -2J \sum_{i=1}^{6} \hat{S}_i \cdot \hat{S}_{i+1} \qquad (2)$$

where J refers to the isotropic magnetic exchange interaction for first-neighbor atoms of the Cu_6 or Mn_6 hexagon, and $\hat{S}_i$ is the operator for the component of the spin vector, **S**. Attempts to fit the data for **1** and **2** were made using a full-matrix diagonalization approach. The spin wave functions for the Cu_6 hexagon are derived from the basis set $|M_{S1}, M_{S2}, M_{S3}, M_{S4}, M_{S5}, M_{S6}\rangle$, where M_{Si} is the microstate corresponding to the ith (i = 1, ..., 6) ion. When $M_{Si} = +^1/_2$ and $-^1/_2$ for each Cu^{2+} are

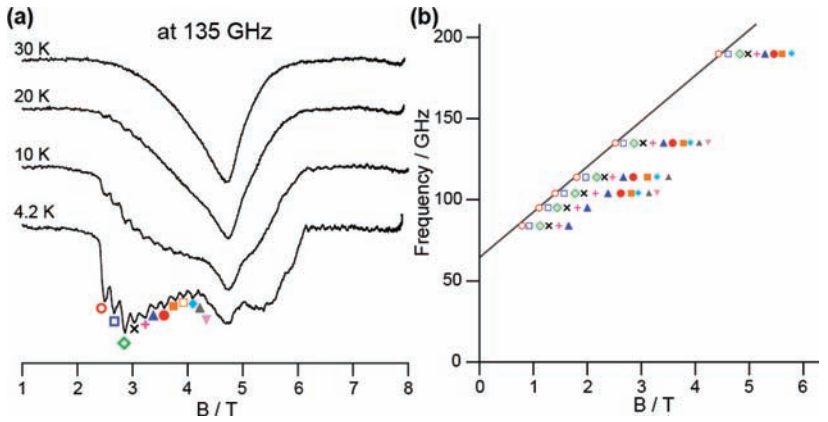

Figure 11. HFESR spectra (a) collected over the temperature range 4.2−30 K at 135 GHz and frequency-dependence diagram (b) for the easy-axis orientation peaks at 4.2 K between 81.5 and 190 GHz for **3**. The solid line fitted for the lowest field peaks gives the zero-field offset value of 67 GHz, which is used for the estimation of the D value.

dx.doi.org/10.1021/ic202513q | Inorg. Chem. 2012, 51, 4606−4619

respectively represented by 0 and 1, thus, the spin wave functions for all the up-spins and down-spins of **1** and **2** can be denoted by |0,0,0,0,0,0⟩ and |1,1,1,1,1,1⟩, for example, and the m_S value corresponding to the total spin s is $m_S = \sum_{i=1}^{6} M_{Si} = \pm 3, \pm 2, \pm 1$, and 0. The possible linear combinations of M_{Si} in this case would give the complete set of 2^6 (=64) eigenfunctions, $|\phi_k\ (k = 1, 2, ..., 64)\rangle$ ($|\phi_1\rangle \equiv |0,0,0,0,0,0\rangle$ and $|\phi_{64}\rangle \equiv |1,1,1,1,1,1\rangle$, for example). The operator of the exchange interactions can be manipulated using the escalator operators ($S_i^+ \equiv S_{ix} + iS_{iy}$ and $S_i^- \equiv S_{ix} - iS_{iy}$) as follows:

$$\begin{aligned}\hat{H}_{\text{exchange}} = &-2J[(S_{1z}S_{2z} + S_{2z}S_{3z} + S_{3z}S_{4z} + S_{4z}S_{5z} \\ &+ S_{5z}S_{6z} + S_{6z}S_{1z}) \\ &+ 1/2(S_1^+S_2^- + S_1^-S_2^+ + S_2^+S_3^- \\ &+ S_2^-S_3^+ + S_3^+S_4^- + S_3^-S_4^+ + S_4^+S_5^- \\ &+ S_4^-S_5^+ + S_5^+S_6^- + S_5^-S_6^+ + S_6^+S_1^- \\ &+ S_6^-S_1^+)] \end{aligned} \quad (3)$$

Thus, one can construct the 64 × 64 Hamiltonian matrix corresponding to the Hamiltonian in eq 3 with the matrix elements ($\langle\phi_i|\hat{H}_{ex}|\phi_j\rangle$). The energy eigenvalues calculated by the full-matrix diagonalization approach are shown in Table 2,

Table 2. Energy Levels of Eigenstates Obtained by Exact Calculations Using the Heisenberg Hamiltonian, Eq 2, for the Cu_6 Hexagon Ring

spin multiplets	degeneracy	energy value
$S = 0$	1	$(5+\sqrt{13})J$
$S = 1$	1	$(5+\sqrt{5})J$
$S = 0$	1	$6J$
$S = 1$	2	$(7+\sqrt{17})J/2$
$S = 1$	2	$5J$
$S = 0$	2	$4J$
$S = 2$	1	$4J$
$S = 2$	2	$3J$
$S = 1$	1	$(5-\sqrt{5})J$
$S = 1$	1	$2J$
$S = 1$	2	$(7-\sqrt{17})J/2$
$S = 0$	1	$(5-\sqrt{13})J$
$S = 2$	2	J
$S = 3$	1	0

where the energy levels for the excited spin-multiplets are depicted by the energy separations from the lowest-lying $S = 3$ state, together with their degeneracy. The energy pattern is in good agreement with the one calculated as a Cu_6-ring model for the magnetic properties of $BaCuO_{2+x}$[19] and also the one obtained by use of the MAGPACK software.[20]

Since it is apparent that the sublevels produced by ZFS for the lowest-lying $S = 3$ state influence the magnetization of the Cu_6 hexagon at lower temperature (Figures 7 and 8), the $S_z = \pm3, \pm2, \pm1$, and 0 levels of the $S = 3$ state were taken into account in the ground state energy (with their energy separation of $|D|S_z^2$). By employing $D = -0.147$ and -0.145 cm^{-1} (Figure 9) for **1** and **2**, respectively, and taking the $S_z = \pm2$ level as an energy origin for the lowest-lying $S = 3$ state, thus, an expression of χ_M for the χ_MT versus T (Figure 3) fitting can be given by eq 4:

$$\begin{aligned}\chi_M = &(2N\mu_B^2g^2/kT)\{4 + \exp(-3|D|/kT) \\ &+ 9\exp(5|D|/kT) + 10\exp(-a/T) + \exp(-2a/T) \\ &+ 10\exp(-3a/T) + 5\exp(-4a/T) + 2\exp(-5a/T) \\ &+ 2\exp(-1.438a/T) + \exp(-2.764a/T) \\ &+ 2\exp(-5.562a/T) + \exp(-7.236a/T)\} \\ &/\{2 + 2\exp(-3|D|/kT) + \exp(-4|D|/kT) \\ &+ 2\exp(5|D|/kT) + 10\exp(-a/T) + 3\exp(-2a/T) \\ &+ 10\exp(-3a/T) + 7\exp(-4a/T) + 6\exp(-5a/T) \\ &+ \exp(-6a/T) + \exp(-1.394a/T) \\ &+ 6\exp(-1.438a/T) + 3\exp(-2.764a/T) \\ &+ 6\exp(-5.562a/T) + 3\exp(-7.236a/T) \\ &+ \exp(-8.606a/T)\} \quad \text{with} \quad a = J/k \end{aligned} \quad (4)$$

As shown by the red solid lines in Figure 3a and Supporting Information Figure S2, the χ_MT data above the ordering temperature (Figure 4) could be well reproduced using eq 4, with the values of $J = +29.5$ cm^{-1} (+42.4 K) and $g = 2.3$, with the agreement factor $R = [\sum\{(\chi_MT)_{calcd} - (\chi_MT)_{obsd}\}^2/\sum\{(\chi_MT)_{obsd}\}^2] = 1.9 \times 10^{-3}$, for **1** and $J = +61.0$ cm^{-1} (+87.9 K) and $g = 2.0$, with $R = 3.0 \times 10^{-4}$, for **2**.[21] The decrease in the χ_MT values at lower temperatures of $T < 7$ K for the Cu_6 hexagon is associated with the combined effects of the Zeeman effect inside the magnetic field and the ZFS experienced by the $S = 3$ ground state, which are not included in the above calculation. Neither model still accounted for this decrease in the χ_MT values in the low temperature range of <7 K (of the cusp temperature).

Although it is basically possible to find analytical expressions of the numerical calculations of eigenenergies through diagonalization also for the Mn_6 hexagon (with the overall degeneracy of $6^6 = 46656$) for **3** and **4**, we employed the Kambe vector coupling method/Van Vleck's approximation (which was used for **3**) due to limitations of our computer memory.[1,22,23] Thus, the best fitting parameters obtained by a simulation of the χ_MT versus T curve in the range 1.8−300 K for **4** were $J = -0.07$ cm^{-1} (−0.09 K) and $g = 1.9$ with $R = 1.2 \times 10^{-4}$, as shown by the red solid line in Figure 3b. Table 3 summarizes the J, g (as the average for all the spin-multiplets), and R values obtained by the fitting of χ_MT-T curves for **1**−**4**, together with the results ($g_\parallel$, $g_\perp$, and D values) obtained by HFESR spectroscopy for the $S = 3$ ground states of **1** and **2** and the $S = 15$ ground state of **3**. The ferromagnetic interaction within the Cu_6 hexagon is strong compared with that of the Mn_6 hexagon, and the interaction for **2** is approximately twice as strong as that for **1**. It is notable that the weak ferromagnetic interaction of $J = +0.14$ cm^{-1} (+0.20 K) for **3** within the Mn_6 hexagon is changed to the weak antiferromagnetic interaction for **4**.

DISCUSSION

Magnetostructural Correlations. For the structural and magnetic properties of di-μ-oxo-copper(II) dimers with nearly planar Cu_2O_2 configuration, a linear correlative relationship

dx.doi.org/10.1021/ic202513q | Inorg. Chem. 2012, 51, 4606−4619

Table 3. Best-Fitting Magnetic Interaction Parameters Obtained from Simulation of the $\chi_M T-T$ Curve for 1−4 and the ESR Parameters Obtained for 1−3

	1	2	3 (ref 1)	4
J in cm^{-1} [a]	+29.5	+61.0	+0.14	−0.07
g [b]	2.3	2.0	2.2	1.9
$R_{\chi T}$ [c]	1.89×10^{-3}	3.02×10^{-4}	3.6×10^{-4}	1.2×10^{-4}
$g_{\parallel}$ [d]	2.30	2.29	2.03	
$g_{\perp}$ [d]	2.19	2.20		
$\langle g \rangle$ [e]	2.27	2.23		
D in cm^{-1}	−0.147	−0.145	−0.077	

[a]The fittings were done by simulating the $\chi_M T-T$ curves in the ranges 7−300 K (for **1** and **2**) and 1.8−300 K (**3** and **4**). [b]Averaged value for all the spin multiplets. [c]Agreement factor. [d]Values for the spin ground states (S = 3 for **1** and **2**; and S = 15 for **3**). [e]$\langle g \rangle \geq (g_{\parallel} + 2g_{\perp})/3$.

(indicated by eq 5) between the Cu−O−Cu bridge angle (ϕ) and the exchange parameter ($2J$) has been shown.[24]

$$2J = -74.53\phi + 7270\ \text{cm}^{-1} \quad (5)$$

This predicts ferromagnetic and antiferromagnetic coupling for the Cu−O−Cu angles smaller and larger than 97.5°, respectively. Although the prediction of the ferromagnetic coupling for **1** (with ϕ = 94.9°) and **2** (with ϕ = 95.3°) is along with the above correlation, the observed ferromagnetic coupling magnitudes seem to be deviated from the values (98.6 and 83.6 cm^{-1}) calculated from eq 5. Also, for the di-μ-oxo-copper(II) dimers with nonplanar Cu_2O_2 configuration, a linear correlative relationship (indicated by eq 6) between the Cu···Cu distance (d) and $2J$ has been shown.[24]

$$2J = -4508d + 13018\text{cm}^{-1} \quad (6)$$

The values of d = 2.94 and 2.91 Å for **1** and **2** predict antiferromagnetic coupling magnitudes (due to d > 2.89 Å) of J = −117.8 and −50.1 cm^{-1}, respectively, which disagree with the observed values (J = 29.5 and 61.0 cm^{-1}, for **1** and **2**, respectively) of the ferromagnetic coupling interaction (Table 3). Therefore, it is meaningful to investigate the magnetostructural correlations on the basis of the structural motifs of the Cu_6 (or Mn_6) hexagon.

As shown in Table 1, each μ_3-O atom in the M_6 hexagon is located nearly on its coordination metal's Cu_2W- or Mn_2W-triangle plane (at 0.07, 0.04, 0.15, and 0.12 Å on average above the M_2W triangle plane for **1**−**4**, respectively), while each magnetic M atom is significantly distant (0.43, 0.40, 0.67, and 0.63 Å above the plane for **1**−**4**, respectively) from the least-squares $(\mu_3\text{-O})_4$ plane in the $ClMO_4$ square pyramid. Since the Cu−O(μ_3)−Cu bond angle (95° for **1** and **2**) is close to 90° and the Mn−O(μ_3)−Mn bond angle (100° and 99° for **3** and **4**, respectively) is close to 100°, the orthogonality between the two O atomic orbitals in the Cu−O−Cu bond is higher than that in the Mn−O−Mn bond, suggesting a significant mixing of s-character into 2p orbitals for the μ_3-O atom orbitals in the Mn−O−Mn bond.

A larger ferromagnetic exchange coupling of **2** compared with **1** is associated with the fact that six Cu atoms in six edge-shared $Cu(\mu_3\text{-O})_4$ square-pyramids ring for **2** form the $Cu_6(\mu_3\text{-O})_{12}$ cylindrical geometry together with 12 μ_3-O atoms, if we note a similarity in diameters (5.81 and 5.83 Å) of the $(\mu_3\text{-O})_6$ and Cu_6 hexagon rings in addition to the shortest location (0.4 Å) of the Cu atom above the least-squares $(\mu_3\text{-O})_4$ plane (Figure 1 and Table 1). In other words, a smaller ferromagnetic exchange coupling of **1** arises from the out-of-cylinder deviation of the Cu atoms in the $Cu_6(\mu_3\text{-O})_{12}$ hexacapped hexagonal prism due to the structural constraints imposed by the binding of α-B-$[SbW_9O_{33}]^{9-}$ to the Cu_6 hexagon, as indicated by a larger deviation of the ring diameter (5.88 Å) for the Cu_6 hexagon ring from that (5.79 Å) for the $(\mu_3\text{-O})_6$ hexagon rings. The ferromagnetism for the $Cu_6(\mu_3\text{-O})_{12}$ least-squares cylinder can be rationalized by the polarization mechanism based on the point-dipole approximation, as demonstrated in Figure 12. In the planar

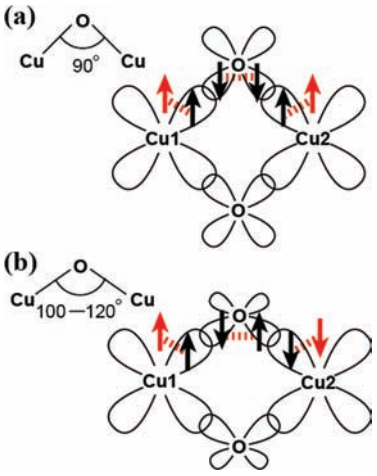

Figure 12. Schematic mechanistic presentation of ferromagnetic (a) and antiferromagnetic (b) interaction couplings between paramagnetic electrons on two Cu atoms in the planar $Cu(1)O_2Cu(2)$ biradical. The paramagnetic electron spin (denoted by red arrow) is located in $d_{x^2-y^2}$* orbital electrons, and related bonding electron spins (denoted by black arrows) are located on both $d_{x^2-y^2}$ and p orbitals superimposed on both Cu and O atoms.

$Cu(1)O_2Cu(2)$ biradical with the Cu−O−Cu bond angle of 90°, Cu−O bonds are formed by spin-pairing of the electrons in the Cu $d_{x^2-y^2}$ and O $2p_x$ (or $2p_y$) orbitals, with the unpaired electron being in the excited $d_{x^2-y^2}$* orbital on the Cu atom. For the isolated Cu(1)−O bond there is no *a priori* preference for a particular spin alignment. Introduction of the odd electron into the Cu $d_{x^2-y^2}$* orbital gives rise to an energetically more favorable situation when the electron in the Cu $d_{x^2-y^2}$ orbital is aligned parallel to the unpaired electron than when the electron are antiparallel (Hund's principle), due to the high orthogonality between the $d_{x^2-y^2}$* and $d_{x^2-y^2}$ orbitals. By the Pauli principle the electron formally in the O $2p_x$ orbital must be antiparallel to that in the $d_{x^2-y^2}$ orbital and, hence, also antiparallel to the unpaired electron on Cu(1). Consequently, there will be a net unbalance of spin at the O $2p_x$ orbital and a negative spin-density will be observed. The same is true for the Cu(2)−O bond: the negative spin-density at the O $2p_x$ orbital gives rise to the energetically more favorable situation when the electron in the O $2p_y$ orbital is aligned with the negative spin-density by Hund's principle, and consequently, the unpaired electron in the excited $d_{x^2-y^2}$* orbital on the Cu(2) atom is aligned parallel to that on the Cu(1) atom. Such a situation leads to the ferromagnetic exchange coupling between Cu(1) and Cu(2) paramagnetic electrons (Figure 12a). When the Cu−O−Cu bond angle in the planar $Cu(1)O_2Cu(2)$ biradical increases from 90° to 120°, s-character is introduced into the O bonding orbitals of pure 2p type to sp^2 or sp^3 hybrid type. At an intermediate stage, two bonding orbitals of the O atom in

dx.doi.org/10.1021/ic202513q | Inorg. Chem. 2012, 51, 4606−4619

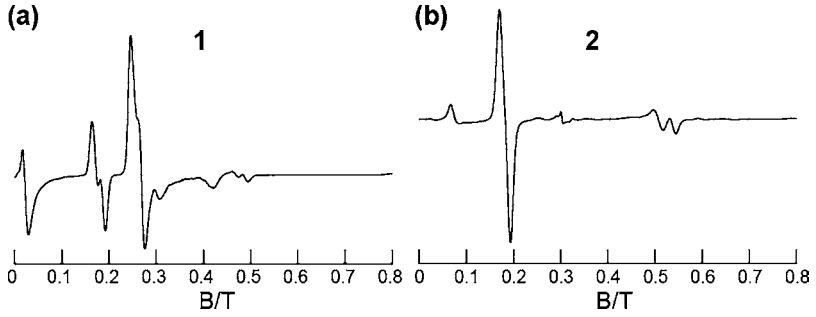

Figure 13. X-Band ESR spectra of **1** (a) and **2** (b) powder samples at 4.5 K.

Cu−O bonds are built from some s-character on the O atom. Under these circumstances, electrons on the O atom tend to pair with their spins antiparallel, and hence the unpaired electron on Cu(2) is aligned antiparallel to that on Cu(1). Consequently, a net antiferromagnetic coupling between the Cu(1) and Cu(2) paramagnetic electrons will be observed, as shown in Figure 12b. In this model, therefore, as the Cu−O−Cu bond angle for the planar $Cu(1)O_2Cu(2)$ biradical increases from 90° (due to 2p orbital) to 120° (due to sp^2 through sp^3 hybrids), the originally ferromagnetic coupling will decrease to zero and then the antiferromagnetic coupling will increase, as revealed by the strong antiferromagnetic coupling (J = −99.1 cm^{-1}) between the two Cu_{int} sites (with the Cu_{int}−$O(sp^3)$−Cu_{int} bond angle of 102.6°) in the rhomblike Cu_4-tetragon for $[n\text{-}BuNH_3]_{12}[Cu_4(GeW_9O_{34})_2]\cdot 14H_2O$.[6]

To understand the different natures of the exchange interaction in **3** (ferromagnetic) and **4** (antiferromagnetic) for the Mn_6 hexagons, it is important to take into account the favorable electron-pairing with their spins antiparallel between the two bonding orbitals on the μ_3-O atom due to a large Mn−O−Mn bond angle (100°) compared with the Cu−O−Cu bond angle (95°), which leads to a decrease of the ferromagnetic exchange interaction between two Mn sites (as exemplified by the planar CuO_2Cu moiety in Figure 12b). In addition, the Mn_6 hexagon ring diameter (6.50 and 6.46 Å) for **3** and **4** is much larger than the $(\mu_3\text{-}O)_{12}$ cylinder diameter (5.94 and 5.99 Å, respectively). Therefore, the out-of-plane deviation of the $Mn(\mu_3\text{-}O)_2Mn$ moiety of the two edge-shared $ClMnO_4$ square pyramids in the Mn_6 hexagon plays a relevant role in the decrease in the ferromagnetic interaction: for **3** the dihedral angle between the two $Mn_2(\mu_3\text{-}O)$ triangle planes in the $Mn(\mu_3\text{-}O)_2Mn$ moiety was 166.6°, which was larger than that for **4** (163.4°). From this perspective, as the out-of-plane deviation of the $Mn(\mu_3\text{-}O)_2Mn$ least-squares plane increases, the originally ferromagnetic exchange interaction will drastically decrease (as observed for **3**) by the antiferromagnetic contribution arising from the large Mn−O−Mn bond angle, and then the largest deviation for **4** leads to net antiferromagnetic coupling. This is due, of course, to the fact that an observed J value is the net sum of the ferro- and antiferromagnetic contributions. In the above model, thus, the weak ferromagnetic and antiferromagnetic exchange interactions observed in **3** and **4**, respectively, can be nicely understood.

Negative Sign and Magnetic Dipole−Dipole Interaction for *D*. The x-band ESR data at the lowest frequency are not appropriate for the estimation of D. Figure 13 shows 9.1 GHz-ESR spectra of **1** (a) and **2** (b) powder samples at 4.5 K, which indicate complicated absorption lines around 0.02−0.08, 0.17−0.19, 0.25−0.31, and 0.39−0.49 T. The strong transition around 0.17−0.19 T for **2** has been temporarily assigned to the transition between the excited levels, probably $m_s = +2 \rightarrow m_s = +1$ or $m_s = -1 \rightarrow m_s = 0$ for the $S = 3$ ground state, on the basis of a 0.18-T singlet line of the single crystal ESR spectrum at 77 K.[1] For the similar Cu_6 hexagon (with a first-neighboring Cu···Cu distance of 2.79 Å and an average Cu−O−Cu bond angle of 92.8° in the range 91.5−94.6°) in $[(PhSiO_2)_6Cu_6(O_2SiPh)_6]\cdot 6EtOH$ (with J = +21.0 cm^{-1}), an approximately twice as high and positive value of D (= +0.3 cm^{-1}) has been estimated by a study of low-temperature 9.25- and 245-GHz ESR spectra of the polycrystalline state:[8a] the near zero field transition observed on the 9.25-GHz ESR spectrum has been assigned to the two lowest-lying levels of $m_s = 0$ and ±1 (with a D splitting) as $D > 0$, and thereby the intensive lines observed at lower fields in the 245-GHz HFESR spectra shift their spectral weight toward transitions occurring at higher fields with an increase of the temperature. As shown in Figure 13, however, the fact that the near zero field peak for **1** and **2** is unlikely to give the broad nature due to the multiple transitions of $g\mu_B B \approx |D|$ precludes the possibility of $D > 0$. Also, the observation of QTM at the crossed field (zero filed) for the $S_z = \pm m_s$ levels for **1** and **2** at 0.5 K (Figure 8) excludes this possibility. The QTM resonances around 0.13 T (0.14 cm^{-1}) and 0.15 T (0.16 cm^{-1}) for **1** and **2** respectively reveal a reasonable agreement with the $|D|$ values (0.147 and 0.145 cm^{-1}) obtained from HFESR spectra, if $g = (g_z + 2g_x)/3 = 2.23$ for **1** and **2** is employed. Furthermore, the weak QTM peak around 0.28 T (0.29 cm^{-1}) for **2** corresponds to the Zeeman crossed field ($2|D|$) between the $S_z = +3$ excited sublevel and the $S_z = -1$ sublevel. Together with the QTM peak observed at zero field (inset in Figure 8b), thus, the three resonances observed (around 0, 0.15, and 0.28 T in Figure 8b) for **2** can be explained in terms of QTM at $k|D|$ (k = 0, 1, and 2) arising from Zeeman-crossed-fields of $S_z = +3$ with $S_z = -3$, −2, and −1 sublevels, which is along with the spin-parity dependent tunneling of the magnetization allowed in integer spin systems.[25] One can note that there are extra resonances observed in the hysteresis measurements for **1** and **2** (Figure 8): ones at 0.07 and 0.20 T for **1** and at 0.23 T for **2**. The observation of these extra resonances is a manifestation of the other magnetic structures of the molecules as a result of a weaker exchange coupling involving second- (with separations of 5.088 and 5.045 Å for **1** and **2**, respectively) and third- (5.876 and 5.825 Å) neighbor interactions between paramagnetic Cu^{II} ions within the Cu_6 hexagon. Thus, the molecules for **1** and **2** may behave as mixtures of ferromagnetically exchange-coupled $S = 3$ states with different D values which generate the observed extra resonances.[18,26]

Finally we discuss an origin of D of the Cu_6 hexagon. The Cu_6 hexagon is assumed to be in an idealized D_{6h} symmetry and to consist of three sets of the isolated binuclear edge-shared

dx.doi.org/10.1021/ic202513q | Inorg. Chem. 2012, 51, 4606−4619

$ClCuO_4$ (or $ClMnO_4$) pyramids for simplification. By using D tensors (with tensor components of $D_{XX} = D_{YY} = -D$ and $D_{ZZ} = +2D$) in the coordinate frame for ZFS in the hexagon coordinate XYZ system, where Y-axis coincides with the virtual 6-fold axis of the Cu_6 hexagon ring, we can estimate the magnetic dipolar interaction (D_{dd} in cm^{-1}). Since D_{dd} between two magnetic centers for the binuclear moiety is given by the equation[9]

$$D_{dd} = (0.325g^2/d^3)(|1 - 3\cos^2\theta|) \quad (7)$$

where d (in Å unit) is the intermagnetic distance and θ is the angle between the d vector and the magnetic field direction,[27] the tensor components (D_{XX}, D_{YY}, and D_{ZZ}) for the hexagon ring (comprising three binuclear magnetic centers) are calculated by using the g values obtained from the above HFESR spectra for **1**−**3**, as follows:

$$|D_{XX}| = (0.325g_x^2/d^3)(|1 - 3\cos^2(0)| + |1 - 3\cos^2(\pi/3)| + |1 - 3\cos^2(\pi/3)|$$

$$|D_{YY}| = (0.325g_y^2/d^3)(|1 - 3\cos^2(\pi/2)| + |1 - 3\cos^2(\pi/2)| + |1 - 3\cos^2(\pi/2)|)$$

$$|D_{ZZ}| = (0.325g_z^2/d^3)(|1 - 3\cos^2(\pi/2)| + |1 - 3\cos^2(\pi/6)| + |1 - 3\cos^2(\pi/6)|)$$

Table 4 lists the calculated D_{dd} values ($=^1/_4(|D_{XX}| + |D_{YY}| + |D_{ZZ}|)$), together with values of d for **1**−**3**. The D_{dd} values obtained for **1**−**3** are in good agreement with the values of $|D|$ obtained from the HFESR measurements (Table 3). Plausible other interactions of the pseudodipolar term[28] originating in the spin−orbit coupling, and the Dzyaloshinky−Moriya (DM) term[23] may contribute to the ZFS parameter D. However, these interactions approximately estimated for the Cu_6 (or Mn_6) hexagon rings disagreed with the observed $|D|$: D_{pseudo} (0.012, 0.015, and 0.0003 cm^{-1}) and D_{DM} (0.073, 0.063, and 0.003 cm^{-1}) for **1**−**3**, respectively. This implies that both pseudodipolar and DM terms are insensitive to D in the present M_6 hexagon system. Thus, it is possible at least to say that the primary contribution to the D value for the $S = 3$ ground state comes from the magnetic dipole−dipole interaction between the electrons located on the magnetic sites in the Cu_6 hexagon.

Table 4. Magnetic Dipolar Interaction (D_{dd} in cm^{-1}) and Its Tensor Components Estimated for 1−3

	1	2	3
d in Å unit[a]	2.938	2.913	3.248
$\|D_{XX}\|$	0.1537	01505	0.0977
$\|D_{YY}\|$	0.1843	0.1806	0.1173
$\|D_{ZZ}\|$	0.2352	0.2434	0.1368
D_{dd}[b]	0.1433	0.1436	0.0880

[a]Intermagnetic distance (corresponding to first-neighboring M···M distance in Table 1). [b]$D_{dd} = {}^1/_4(|D_{XX}| + |D_{YY}| + |D_{ZZ}|)$.

■ ASSOCIATED CONTENT

Supporting Information

CIF data (with checkCIF/PLATON reports) for **1** and **4**, Figure S1 of 135 GHz ESR spectra in the range 4.2−30 K for **4**, and Figure S2 of the $\chi_M T - T$ plot in the range 1.8−300 K under 0.1 T for **2**. This material is available free of charge via the Internet at http://pubs.acs.org.

■ AUTHOR INFORMATION

Corresponding Author

*E-mail and telefax: yamase.modevice@nifty.com and +81-76-267-0468.

Notes

The authors declare no competing financial interest.

■ ACKNOWLEDGMENTS

This work was supported by Grants-in-Aid for Scientific Research, Nr. 17002006, from the Ministry of Education, Science, Sports, and Culture.

■ REFERENCES

(1) Yamase, T. E.; Fukaya, K.; Nojiri, H.; Ohshima, Y. *Inorg. Chem.* **2006**, *45*, 7698.
(2) (a) Müller, A.; Peter, F.; Pope, M. T.; Gatteshi, D. *Chem. Rev.* **1998**, *98*, 239. (b) Coronado, E.; Gómez-Garcia, C. J. *Chem. Rev.* **1998**, *98*, 273. (c) Clemente-Juan, J. M.; Coronado, E. *Coord. Chem. Rev.* **1999**, *193*−*195*, 361. (d) Mialane, P.; Dolbecq, A.; Marrot, J.; Rivière, E.; Sécheresse, F. *Chem.—Eur. J.* **2005**, *11*, 1771. (e) Schröder, C.; Nojiri, H.; Schnack, J.; Hage, P.; Luban, M.; Kögerler, P. *Phys. Rev. Lett.* **2005**, *94*, 172505. (f) Bi, L.; Kortz, U.; Nellutia, S.; Stowe, A. C.; van Tol, J.; Dalal, N. S.; Keita, B.; Nadjo, L. *Inorg. Chem.* **2005**, *44*, 896.
(3) Yamase, T.; Ishikawa, E.; Fukaya, K.; Nojiri, H.; Taniguchi, T.; Atake, T. *Inorg. Chem.* **2004**, *43*, 8150.
(4) Choi, K.-Y.; Matsuda, Y.; Nojiri, H.; Kortz, U.; Hussain, F.; Stowe, A. C.; Ramsey, C.; Dalal, N. S. *Phys. Rev. Lett.* **2006**, *96*, 107202.
(5) (a) Ohshima, Y.; Nojiri, H.; Fukaya, K.; Yamase, T. *J. Phys. Conf. Ser.* **2006**, *51*, 195. (b) Fukaya, K.; Yamase, T. *Bull. Chem. Soc. Jpn.* **2007**, *80*, 178. (c) Oshima, Y.; Nojiri, H.; Fukaya, K.; Yamase, T. *J. Phys. Soc. Jpn.* **2008**, *77*, 044706.
(6) Yamase, T.; Abe, H.; Ishikawa, E.; Nojiri, H.; Ohshima, Y. *Inorg. Chem.* **2009**, *48*, 138.
(7) (a) Weakley, T. J. R.; Evans, H. T.; Showell, J. S.; Tourné, G. F.; Tourné, C. M. *J. Chem. Soc., Chem. Commun.* **1973**, 139. (b) Evans, H. T. Jr.; Tourné, G. F.; Tourné, C. M.; Weakley, T. J. R. *J. Chem. Soc., Dalton Trans.* **1986**, 2699. (c) Gómez-García, C. J.; Coronado, E.; Borrás-Almenar, J. *Inorg. Chem.* **1992**, *31*, 1667. (d) Clemente-Juan, J. M.; Andres, H.; Borrás-Alamenar, J. J.; Coronado, E.; Güdel, H.-U.; Aebersold, M.; Kearly, G.; Büttner, H.; Zollinker, M. *J. Am. Chem. Soc.* **1999**, *121*, 10021. (e) Andres, H.; Clemente-Juan, J. M.; Aebersold, M.; Güdel, H.-U.; Coronado, E.; Büttner, H.; Kearly, G.; Melero, J.; Burriel, R. *J. Am. Chem. Soc.* **1999**, *121*, 10028. (f) Clemente-Juan, J. M.; Coronado, E.; Galán-Mascarós, J. R.; Gómez-García, C. J. *Inorg. Chem.* **1999**, *38*, 55. (g) Kortz, U.; Isber, S.; Dickman, M. H.; Ravot, D. *Inorg. Chem.* **2000**, *39*, 2915. (h) Bi, L.-H.; Huang, R.-D.; Peng, J.; Wang, E.-B.; Wang, Y.-H.; Hu, C.-W. *J. Chem. Soc., Dalton Trans.* **2001**, 121. (i) Kortz, U.; Nellutla, S.; Stowe, A. C.; Dalal, N. S.; van Tol, J.; Bassil, B. S. *Inorg. Chem.* **2004**, *43*, 144. (j) Kortz, U.; Nellutla, S.; Stowe, A. C.; Dalal, N. S.; Rauwald, U.; Danquah, W.; Ravot, D. *Inorg. Chem.* **2004**, *43*, 2317.
(8) (a) Rentschler, E.; Gatteschi, D.; Cornia, A.; Fabretti, A. C.; Barra, A.-L.; Shchegolikhina, O. I.; Zhdanov, A. A. *Inorg. Chem.* **1996**, *35*, 4427. (b) Ruiz, E.; Cano, J.; Alvarez, S.; Caneschi, A.; Gatteschi, D. *J. Am. Chem. Soc.* **2003**, *125*, 6791.
(9) Gómez-Garcí, C. J.; Borrás-Almenar Coronado, E.; Ouahab, L. *Inorg. Chem.* **1994**, *33*, 4016.
(10) Clemente-Juan, J. M.; Coronado, E.; Gaita-Ariño, A.; Giménez-Saiz, C.; Chaboussant, G.; Güdel, H.-U.; Burriel, R.; Mutka, H. *Chem.—Eur. J.* **2002**, *8*, 5701.
(11) Kortz, U.; Mbomekalle, I. M.; Keita, B.; Nadjo, L.; Berthet, P. *Inorg. Chem.* **2002**, *41*, 6412.

(12) Mbomekalle, I. M.; Keita, B.; Nierlich, M.; Kortz, U.; Berthet, P.; Nadjo, L. *Inorg. Chem.* **2003**, *42*, 5143.
(13) Bösing, M.; Loose, L.; Pohlman, H.; Krebs, B. *Eur. J. Chem.* **1997**, *3*, 1232.
(14) Tourné, C.; Revel, A.; Tourné, G.; Vendrell, M. *C. R. Acad. Soc. Paris, Ser. C* **1973**, *t277*, 643. IR (KBr disk): 931 (m), 903 (s), 781 (s), 725 cm^{-1} (s).
(15) Further details on the crystal structure investigations are given in CIF files as Supporting Information.
(16) O'Conner, C. J. *Prog. Inorg. Chem.* **1982**, *29*, 203.
(17) Nojiri, H.; Choi, K.-Y.; Kitamura, N. *J. Magn. Magn. Mater.* **2007**, *310*, 1468.
(18) Shah, S. J.; Ramsey, C. M.; Heroux, K. J.; DiPasquale, A. G.; Dalal, N. S.; Rheingold, A. L.; Barco, E.; Hendrickson, D. N. *Inorg. Chem.* **2008**, *47*, 9569.
(19) Wang, Z. R.; Johnston, D. C.; Miller, L. L.; Vaknin, D. *Phys. Rev. B* **1995**, *52*, 7384. In ref 19 there is a mistake: a value (=2) of the degeneracy for the second $S = 1$ state as the exact results in Figure 10 should be corrected to one (=1), as shown by the present result. Also, the approximate energy levels given by the Van Vleck's approximation on the same figure should be multiplied by 2.5.
(20) Zamstein, N.; Tarantul, A.; Tsukerblat, B. *Inorg. Chem.* **2007**, *46*, 8851.
(21) The Kambe vector coupling method/Van Vleck's approximation did not sufficiently fit the data in the whole temperature range 7−300 K:[1] the simulation of the $\chi_M T - T$ curve at two ranges of 7−300 K and 70−300 K by a use of Van Vleck's approximation for **2** has provided a lower J value, $J = +18.0$ cm^{-1} (+25.9 K), and $g = 1.99$ with $R = 3.9 \times 10^{-3}$, and $J = +8.82$ cm^{-1} (+12.7 K) and $g = 2.27$ with $R = 2.7 \times 10^{-5}$ as the best fitting parameters, respectively.
(22) Kambe, K. *J. Phys. Soc. Jpn.* **1950**, *5*, 48.
(23) Boča, R. *Theoretical foundations of molecular magnetism"*; Current Methods in Inorganic Chemistry, Vol. 1; Elsevier Science: Amsterdam, 1999.
(24) Crawford, V. H.; Richardson, H. W.; Wasson, J. R.; Hodgson, D. J.; Hatfield, W. E. *Inorg. Chem.* **1976**, *15*, 2107.
(25) Wernsdorfer, W.; Bhaduri, S.; Boskovic, C.; Christou, G.; Hendrickson, D. N. *Phys. Rev. B* **2002**, *65*, 180403(R).
(26) Ramsey, C. M.; Del Barco, E.; Hill, S.; Shah, S. J.; Beedle, C. C.; Hendrickson, D. N. *Nat. Phys.* **2008**, *4*, 277.
(27) Stevens, K. W. H. *Proc. R. Soc. (London)* **1952**, *A214*, 227.
(28) Bleaney, B.; Bowers, K. D. *Proc. R. Soc. (London)* **1952**, *A214*, 451.